Author Manuscript

Author Manuscript

Author Manuscript

Author Manuscript

HHS Public Access

Author manuscript

Phys Med Biol. Author manuscript; available in PMC 2019 July 03.

Published in final edited form as:

Phys Med Biol. ; 64(6): 065007. doi:10.1088/1361-6560/ab03e2.

Functional imaging of tumor vasculature using iodine and gadolinium-based nanoparticle contrast agents: a comparison of spectral micro-CT using energy integrating and photon counting detectors

C T Badea[1,4,5], **D P Clark**[1], **M Holbrook**[1], **M Srivastava**[3], **Y Mowery**[2], and **K B Ghaghada**[3]

[1]Department of Radiology, Center for In Vivo Microscopy, Duke University, Durham, NC 27710, United States of America

[2]Department of Radiation Oncology, Duke University, Durham, NC 27710, United States of America

[3]Singleton Department of Pediatric Radiology, Texas Children's Hospital, Houston, TX 77030, United States of America

[4]http://civm.duhs.duke.edu/

[5]Author to whom any correspondence should be addressed.

Abstract

Advances in computed tomography (CT) hardware have propelled the development of novel CT contrast agents. In particular, the spectral capabilities of x-ray CT can facilitate simultaneous imaging of multiple contrast agents. This approach is particularly useful for functional imaging of solid tumors by simultaneous visualization of multiple targets or architectural features that govern cancer development and progression. Nanoparticles are a promising platform for contrast agent development. While several novel imaging moieties based on high atomic number elements are being explored, iodine (I) and gadolinium (Gd) are particularly attractive because of their existing approval for clinical use. In this work, we investigate the *in vivo* discrimination of I and Gd nanoparticle contrast agents using both dual energy micro-CT with energy integrating detectors (DE-EID) and photon counting detector (PCD)-based spectral micro-CT. Simulations and phantom experiments were performed using varying concentrations of I and Gd to determine the imaging performance with optimized acquisition parameters. Quantitative spectral micro-CT imaging using liposomal-iodine (Lip-I) and liposomal-Gd (Lip-Gd) nanoparticle contrast agents was performed in sarcoma bearing mice for anatomical and functional imaging of tumor vasculature. Iterative reconstruction provided high sensitivity to detect and discriminate relatively low I and Gd concentrations. According to the Rose criterion applied to the experimental results, the detectability limits for I and Gd were approximately 2.5 mg ml^{-1} for both DE-EID CT and PCD micro-CT, even if the radiation dose was approximately 3.8 times lower with PCD micro-CT. The material concentration maps confirmed expected biodistributions of contrast agents in the blood, liver, spleen and kidneys. The PCD provided lower background signal and better

cristian.badea@duke.edu.

Author Manuscript Author Manuscript Author Manuscript Author Manuscript

simultaneous visualization of tumor vasculature and intratumoral distribution patterns of nanoparticle contrast agent compared to DE-EID decompositions. Preclinical spectral CT systems such as this could be useful for functional characterization of solid tumors, simultaneous quantitative imaging of multiple targets and for identifying clinically-relevant applications that benefit from the use of spectral imaging. Additionally, it could aid in the development nanoparticles that show promise in the developing field of cancer theranostics (therapy and diagnostics) by measuring vascular tumor biomarkers such as fractional blood volume and the delivery of liposomal chemotherapeutics.

Keywords

computed tomography; preclinical; spectral; liposomes; nanoparticles; cancer; photon counting detector

1. Introduction

Spectral x-ray CT (e.g. dual energy CT) using heavy-metal nanoparticle (NP) contrast agents can facilitate *in vivo* understanding of tumor biology and its relationship to the delivery of NPs for therapy. For instance, two NP contrast agents can be used simultaneously to image tumor ‘leakiness’ and to denote tumor vasculature at high spatial resolution (Clark et al 2013). Our group has been a pioneer in the preclinical development of DE micro-CT for cancer imaging (Badea et al 2011, 2012b, Ashton et al 2016). Unfortunately, the contrast sensitivity of DE micro-CT methods is limited by the energy integrating detectors (EIDs) used in most micro-CT instruments. X-rays are composed of photons, and are generally produced with a polychromatic energy spectrum (like visible light). EIDs produce an output signal that is proportional to the detected photon flux, weighted by the photon energy and integrated across the entire photon spectrum. However, heavy-metal contrast agents are differentiable due to spectrally localized changes in x-ray attenuation at characteristic K-edge energies. Thus, the suitability of EIDs for K-edge NP imaging is limited.

Expanding from DE-EID CT to spectral CT using photon counting detectors (PCD) has the potential to improve CT contrast sensitivity (Taguchi and Iwanczyk 2013). PCDs count and bin x-rays into a number of energy bins and eliminate dark noise in the image by rejecting all counts below the signal. Most importantly, spectral PCD-based CT is expected to provide better material separation compared to DE-EID CT. Clinical use of PCDs remains limited due to pulse pile up and charge sharing effects (Taguchi and Iwanczyk 2013), though some clinical prototypes already exist (Li et al 2016). Nevertheless, PCDs could be the next step in CT imaging technology, and their adoption could lead to increases in contrast sensitivity, while reducing radiation exposure during routine CT scans (Symons et al 2017). Preclinical imaging represents an excellent development and testing environment for spectral PCD CT technologies with potential for clinical translation. Preclinical micro-CT may be less affected by pulse pile-up problems than clinical CT, since the flux can be reduced. Many groups, including ours, are therefore developing new prototype PCD micro-CT systems and new contrast agents to explore their capabilities. Currently, there is one commercially available PCD-based micro-CT system, the Medipix All Resolution System (MARS

Author Manuscript Author Manuscript Author Manuscript Author Manuscript

Bioimaging Ltd.; Christchurch, New Zealand) (Anderson et al 2010). The MARS scanner uses the Medipix3 detector chip developed at CERN (Geneva, Switzerland) with charge-summing circuitry to compensate for charge sharing between neighboring detector pixels (Ballabriga et al 2006).

Interestingly, recent improvements in contrast sensitivity have fueled investigations into the development of novel contrast agents, including NP-based platforms, for preclinical molecular CT imaging (Ashton et al 2015). As imaging probes, NPs associated with various targeting strategies can facilitate molecular imaging with CT (Ashton et al 2018). Their ability to package a large payload of imaging moieties enables signal amplification at the target site. Although significant challenges exist due to the low contrast sensitivity of CT relative to nuclear imaging modalities such as PET and SPECT, it is possible to image multiple probes based on different heavy metal (K-edge) materials that are simultaneously present in the body at relatively high spatial resolution.

The aim of the current study is to compare preclinical DE-EID and PCD CT for differentiation of NPs based on two elements suitable for K-edge imaging: gadolinium (Gd) and iodine (I). We utilized liposomes, one of the most extensively studied NP platforms, for the fabrication of NP contrast agents. We have developed and extensively studied Liposomal iodine (Lip-I) contrast agents for CT imaging applications in blood-pool, cancer, and cardiovascular imaging (Annapragada et al 2012, Badea et al 2012a, Starosolski et al 2015, Ghaghada et al 2016). Additionally, we have developed and tested Liposomal Gd (Lip-Gd) contrast agents for MR imaging (Ghaghada et al 2008). Gadolinium has also been used as contrast material for CT (Gierada and Bae 1999); moreover, Gd may have greater potential as a K-edge contrast agent for cadmium telluride (CdTe)-based PCD CT (Muenzel et al 2017). More importantly, both I and Gd are already used as contrast materials in the clinic, unlike other materials that require extensive toxicity studies before being clinically translated. While some PCD and DE-CT comparison has been attempted at the clinical level (Gutjahr et al 2016), to our knowledge, this is the first preclinical study to compare *in vivo* DE-EID and PCD CT imaging and to demonstrate the utility of this methodology for cancer imaging.

2. Material and methods

We begin by introducing the liposomal NP contrast agents used in this work. Short technical descriptions of our dual-source, preclinical DE-EID and PCD CT system setups and our data acquisition are then provided. Based on these details, realistic simulation experiments are conducted to establish limits on the expectations of contrast material decomposition accuracy possible with each system and method. Finally, details are provided for phantom experiments and an *in vivo* micro-CT experiment using a primary mouse model of soft tissue sarcoma.

2.1. Liposomal-based iodine and gadolinium contrast agents for CT

Liposomal-based contrast agents containing I and Gd were fabricated similar to methods described previously (Mukundan et al 2006, Ghaghada et al 2008, Badea et al 2012a). Briefly, a lipid mixture (150 mM) consisting of 1,2-dipalmitoyl-sn-glycero-3-

Author Manuscript Author Manuscript Author Manuscript Author Manuscript

phosphocholine (DPPC), cholesterol, and 1,2-distearoyl-sn-glycero-3-phosphoethanolamine-N-(methoxy (polyethylene glycol)-2000) (DSPE-MPEG 2000) (56:40:4 molar ratio) was dissolved in ethanol. The ethanolic solution was hydrated with either iodixanol solution (550 mg I ml^{-1}), for the preparation of Lip-I, or with gadoteridol (500 mM Gd), for the preparation of Lip-Gd. The hydrated solution was sequentially extruded to obtain liposomes of desired size distribution. The resulting solution was diafiltered to remove un-encapsulated iodixanol/gadoteridol. The size distribution of liposomes in the final formulation was determined by dynamic light scattering (DLS). The I concentration in the final Lip-I solution was quantified by spectrophotometry (λ = 245 nm). The Gd concentration in the final Lip-Gd solution was quantified by inductively-coupled plasma atomic emission spectroscopy (ICP-OES). The final I concentration in the Lip-I formulation was 110 ± 4 mg ml^{-1}, and the final Gd concentration in the Lip-Gd formulation was 20 ± 3 mg ml^{-1}. The average liposome size was 145 ± 6 nm for Lip-I and 219 ± 13 nm for Lip-Gd. The poly-dispersity index for both formulations was less than 0.15.

2.2. Imaging systems

2.2.1. DE-EID Micro-CT—Our dual source micro-CT system used for DE-EID micro-CT imaging has been described in detail previously (Badea et al 2008). The system incorporates two imaging chains capable of independently triggered acquisitions. The system contains two G-297 x-ray tubes (Varian Medical Systems, Palo Alto, CA) with 0.3 mm focal spot size, two Epsilon high-frequency x-ray generators by EMD Technologies (Quebec, Canada), and two flat-panel CsI based detectors (model Dexela 1512CL, PerkinElmer) with 75 μm, isotropic pixels. Data acquisition is controlled by an in-house developed sequencing application written in LabVIEW (National Instruments). The subject is mounted in a vertical cradle and rotated through all projection angles with a circular scanning trajectory. The source to detector and source to object distances were 820 and 679 mm for the first imaging chain and 831 and 680 mm for the second imaging chain. Thus, magnification for the DE-EID CT system was approximately 1.2.

2.2.2. PCD Micro-CT—Our PCD micro-CT system uses a prototype PCD from DECTRIS AG of Baden-Dättwil, Switzerland (https://www.dectris.com/) model SANTIS 0804 ME based on a 1 mm CdTe sensor with 150 μm, isotropic pixels. The PCD has 4 energy thresholds. We use the same type of x-ray source as for the DE-EID micro-CT system. The subject is mounted in a vertical cradle and rotated through all projection angles with a helical scanning trajectory. Data acquisition is controlled by an in-house developed sequencing application written in LabVIEW (National Instruments). The source to detector and source to object distances were 831 mm and 680 mm, respectively (a magnification of ~1.2). To minimize ring artifacts in our reconstructions, we scanned using a helical trajectory with three rotations and vertically translated the object 1.25 cm during scanning. The ring artifacts are caused by pixels with non-linear energy- and time-varying response profiles.

The energy thresholds of the PCD used in this study were set to 25, 34, 50 and 60 keV. We have not subtracted projections between the consecutive energy bins. The first threshold (25 keV) was selected to limit spectral distortions due to charge sharing for low keV photons

Author Manuscript Author Manuscript Author Manuscript Author Manuscript

and to remain well above the detector's noise floor located below 6 keV. The next two thresholds were chosen to image the K-edges of I (33.2 keV) and Gd (50.2 keV). Finally, the last threshold at 60 keV was selected to provide enough counts when imaged with a polychromatic x-ray source at 80 kVp.

2.3. Image reconstruction

To improve the detectability of low concentrations of I and Gd, both DE-EID and PCD CT data were reconstructed using the iterative spectral CT reconstruction framework we have previously described (Clark and Badea 2017). Specifically, we applied the split Bregman method with the add-residual-back strategy (Gao et al 2011) to solve the following optimization problem:

$$X = \underset{X}{\operatorname{argmin}} \frac{1}{2} \sum_e \|RX_e - Y_e\|_2^2 + \lambda \|X\|_{\mathrm{BTV}}, \quad (1)$$

$$\|X\|_{\mathrm{BTV}} : \sum_e \frac{\sum_{i,j} D(i) K(i,j) \mid W(i) X_e(i,j) \mid}{\sum_{i,j} D(i) K(i,j)}, \quad (2)$$

$$K(i,j) = \prod_e \exp\left(- \frac{(W(i) X_e(i,j))^2}{2 m_e^2 \sigma_e^2} \right). \quad (3)$$

This algebraic reconstruction problem solves for the vectorized, reconstructed data, the columns of X, for each sampled threshold (kVp) simultaneously (indexed by e). The reconstruction for each threshold minimizes the reprojection error (R system projection matrix) relative to the log-transformed projection data acquired at each threshold (the columns of Y). To reduce noise in the reconstructed results, this data fidelity term is minimized subject to the bilateral total variation (BTV) measured within and between thresholds. Specifically, as shown above, BTV is calculated as the weighted sum of image gradients (intensity gradient operator W), where the weights are computed over a local neighborhood (D domain, index i) and summed over the entire image (index j) and energies. To handle varying noise levels and contrast with energy, range weights (kernel K) are determined by intensity gradient magnitudes relative to the noise level (σ_e) and smoothing parameter (m_e) set for each energy. During iterative reconstruction, BTV is reduced by the application of BF. To maximize redundancy between the reconstructed thresholds and, therefore, minimize noise in the material decomposition results, we employed a specific extension of joint BF known as rank-sparse kernel regression (RSKR). RSKR is similar to the equations above, except that a weighted singular value decomposition is performed across the energy dimension prior to filtration to improve performance and to simplify parameter selection. RSKR and our regularization strength scaling strategy to compensate for different noise level between thresholds are detailed in previous work (Clark and Badea

Author Manuscript Author Manuscript Author Manuscript Author Manuscript

2017). All DE-EID and PCD CT phantom and mouse data were reconstructed with the same isotropic voxel size of 123 μm, facilitating the comparison of results.

2.4. Material decomposition

For DE-EID micro-CT, material decomposition of Gd and I was performed after reconstruction and Hounsfield units (HU) conversion. Specifically, decomposition used paired reconstructions at two different kVps ($E1$, $E2$) and solved the following linear system at each voxel:

$$C = A^{-1}b\,. \quad (4)$$

Expanding the linear system in equation (4):

$$\begin{bmatrix} C_I \\ C_{Gd} \end{bmatrix} = \begin{bmatrix} CT_{I,E1} CT_{Gd,E1} \\ CT_{I,E2} CT_{Gd,E2} \end{bmatrix}^{-1} \begin{bmatrix} CT_{E1} \\ CT_{E2} \end{bmatrix}. \quad (5)$$

In this formulation, C is the least-squares solution for the concentration of the I (C_I) and Gd (C_{Gd}) in mg ml^{-1} in the voxel under consideration. A is a constant sensitivity matrix measured in Hounsfield units per contrast agent concentration (HU/mg/ml) for I ($CT_{I,E1}$, $CT_{I,E2}$) and Gd ($CT_{Gd,E1}$, $CT_{Gd,E2}$) at $E1$ and $E2$, respectively. Finally, b is the intensity of the voxel under consideration at $E1$ (CT_{E1}) and $E2$ (CT_{E2}) in Hounsfield units. After finding the solution to the linear system, non-negativity was enforced by setting voxels with negative concentrations of both materials to zero. Voxels with a negative concentration of one material and a positive concentration of the other material were orthogonally projected onto the subspace of positive concentrations. Values for the coefficients of the sensitivity matrix at each energy ($CT_{I,E1}$, $CT_{I,E2}$, $CT_{Gd,E1}$ *and* $CT_{Gd,E2}$) were determined empirically using a calibration phantom as described previously (Clark et al 2013).

To decompose spectral PCD micro-CT data, we also used a post-reconstruction decomposition method. Extending the approach of Alvarez and Macovski (1976) we performed a basis material decomposition:

$$\mu(E) = a_{PE}\mu_{PE}(E) + a_{CS}\mu_{CS}(E) + a_I\mu_I(E) + a_{Gd}\mu_{Gd}(E)\,. \quad (6)$$

Given reconstruction acquired with four energ bins, E, the first two terms describe the energy-dependent attenuation, $\mu(E)$, owing to the photoelectric effect (PE) and Compton scattering (CS). The next two terms are basis functions for K-edge materials, in this case I and Gd. For comparison with the DE data, we also performed a PCD DE decomposition in which the four energy bins were used to solve the overdetermined system of equations with only two unknowns (i.e. I and Gd concentrations). We call this PCD2, while we use the term PCD4 for four basis material decomposition as in equation (6). After decomposition, the

Author Manuscript Author Manuscript Author Manuscript Author Manuscript

material maps are color coded with I in red, Gd in green, PE in blue, and CS in gray. All colored maps are color merged and displayed in ImageJ (https://imagej.nih.gov/ij/).

2.5. Simulations

To better understand the limits of our preclinical spectral CT imaging methods, we have performed x-ray simulations for both DE-EID and PCD-based imaging using Spektr (Siewerdsen et al 2004). The energy dependencies of the attenuation for water and I and Gd solutions are shown in figure 1(A). Note the K-edges of I (33.2 keV) and Gd (50.2 keV). We have recently reported on both simulations and physical phantom experiments to validate the optimal scanning kVps for DE-CT imaging of the Lip-I and Lip-Gd contrast agents (Badea et al 2018). The two energy settings that provided maximum contrast discrimination between I and Gd were determined to be 50 kVp with 0.1 mm Cu filtration and 40 kVp without any filtration. Our model included the spectral response of the CsI scintillator. As shown by figure 1(B), these two x-ray spectral responses are approximately bracketing the K-edge of I at 33.2 keV. We note that with only two EID measurements and with kVps suitable for small animal imaging (i.e. ranging from 40 and 80 kVp), we effectively optimized for only one of the materials (in this case I). CsI (thickness of 0.15 mm) used in the detector's scintillator and the copper filtration are the major determining factors in the increase of I contrast with the 50 kVp spectrum.

Both our simulated and experimental results (Badea et al 2018) have proved that the above kVp settings provide the best combination with the lowest condition number of the material sensitivity matrix used for material decomposition. The condition number is the ratio of the largest and smallest singular values of a matrix, and it quantifies the potential for error amplification (higher values indicate greater potential for error amplification). All of our *in vivo* and simulated DE-EID projection data was corrected for beam hardening prior to reconstruction. The correction, which improves the linearity of attenuation measurements, was calibrated with an acrylic wedge (Zou et al 2011).

We have also simulated the spectral response of the PCD micro-CT (see figure 1(C)). The PCD spectral response included the 80 kVp tungsten based x-ray tube spectrum with 0.1 mm Cu filtration as well as the expected quantum efficiency of detection with 1 mm of CdTe (Radicci et al), but did not model more complex physical phenomena such as charge sharing and pulse pile-up. As shown by figure 1(C), the PCD spectral response has a peak in close proximity to the K edge of Gd (i.e. 50.2 keV).

The DE-EID and PCD-based spectral responses were used in the x-ray imaging forward models to create realistic projections from a digital phantom. We have previously introduced the digital contrast and resolution phantom, which was originally constructed to assess the fidelity of hybrid spectral CT reconstruction (Clark and Badea 2017). The phantom consists of a cylinder of water with a diameter of 4.5 cm, scaled to match the diameter of the cradle used for scanning adult mice. The cylinder is divided into three segments (disks) along the *z*-axis. As shown in figure 2, each disk is dominated by a single contrast material we aim to separate *in vivo*: I (red), calcium (blue), and Gd (green). The materials are present in realistic concentrations for small animal micro-CT—10 mg ml^{-1} of I, 75 mg ml^{-1} of calcium, and 10 mg ml^{-1} of Gd in water (material fraction = 1.0). To provide a visual

Author Manuscript Author Manuscript Author Manuscript Author Manuscript

assessment of spatial resolution, each disk contains a set of line pairs which discretely represent spatial frequencies from 1 to 4.07 line pairs per mm (lp mm)$^{-1}$. To assess the trade-offs in feature detection with feature size and material concentration, a grid of spheres is included within each disk. Along the vertical axis, the diameters of these spheres vary from 1.0 mm to 2.5 mm in increments of 0.5 mm, with some truncation due to discretization. Along the horizontal axis, the concentrations of each disk's material take on the following fractions of the maximum concentration: 1.0, 0.5, 0.25, and 0.1. Additional vials (3.5 mm cylinders) of I, calcium, Gd, and water (invisible) are included below the spheres (material fraction = 0.5) and were used for material sensitivity measurements.

Additional steps were taken to better match the image noise of the *experimental acquisitions*. Specifically, photon counts were adjusted such that when the recorded counts were drawn from a Poisson distribution with a mean equal to the attenuated intensity, the resultant filtered backprojection (FBP) reconstructions reproduced the expected noise standard deviations measured in water. Reference water noise measurements were taken at the center of the physical calibration phantom and were matched to the water vial of the digital phantom. For the DE-EID simulations in the 40 kVp scan, we used 1×10^4 photons/line integral to match a noise standard deviation of 83 HU; in case of the other scan at 50 kVp + Cu filtration, we used 4.5×10^3 photons/line integral to match a noise level of 122.5 HU. For the PCD simulations involving a scan at 80 kVp with Cu filtration, we used 1.25×10^4 photons/line integral, which resulted in noise levels of 91, 124, 237, and 416 HU for the four energy thresholds (25, 34, 50 and 60 keV).

To better model the limited energy resolution of the PCD, we used a Gaussian energy spread function with a standard deviation of 2.5 keV to model non-ideal spectral binning. While simplified, Gaussian smoothing of the spectral binning functions is consistent with pervious experimental measurements of monoenergetic energy-spread functions in CdTe-based PCDs (Schlomka et al 2008, Clark et al 2015). Furthermore, a standard deviation of 2.5 keV reproduced the empirically measured condition number of the material sensitivity matrix for the real PCD system (four materials). Notably, all condition numbers were measured following unit normalization of the sensitivity vectors for each material. In the case of DE-EID, the simulated and measured condition numbers were close: 5.5 in simulations and 4.9 for the experimental scans. The condition number for the PCD4 was 34 in simulations and 37.9 for the experimental scans. By comparison, the condition number in the PCD2 decomposition was 5.58 in simulations and 6.5 in the experimental scans.

2.6. Quantitative evaluation

Several metrics were used to quantitatively evaluate the results of DE-EID and PCD material decomposition using the digital phantom. *Root mean square error* (RMSE) assessed the accuracy of the I and Gd maps and was computed as follows:

$$\mathrm{RMSE} = \sqrt{\frac{1}{n}\sum_{y=1}^{n}([C]_y - [C]_0)^2}, \quad (7)$$

Author Manuscript Author Manuscript Author Manuscript Author Manuscript

where y indexed the voxels, n was the total number of voxels, $[C]_y$ was the measured concentration of C = I or C = Gd in voxel y, and $[C]_0$ was the expected concentration of I or Gd in voxel y.

Contrast to noise ratio (CNR) characterized the detectability of each element within the decomposition maps afforded by the different scans and was computed for I and Gd as follows:

$$\mathrm{CNR} = \frac{|\, m_y - m_b \,|}{\sqrt{\sigma_y^2 + \sigma_b^2}}, \quad (8)$$

where m_y and σ_y^2 refer to the mean and variance measured for one of the two materials (i.e. I or Gd) and m_b and σ_b^2 refer to the mean and variance measured in a background region of interest (the water vial of the phantom). To assess the limits of detectability, the Rose criterion was applied stating that a given concentration of I or Gd could be reliably detected when the CNR was ⩾5 (Rose 1948).

2.7. Phantom experiments

Physical phantom experiments were designed and performed to validate the simulations. First, we used vials of water, I, and Gd to verify that the PCD threshold positions yielded the expected changes in contrast around the K edges of I and Gd. These projections were log transformed and normalized to the attenuation of water to make the K-edge associated contrast enhancements more distinct.

Next, a 3D printed phantom containing solutions of I in water (9.25, 5.3, 3.75 and 2 mg ml^{-1}) and Gd in water (10, 5 and 2.5 mg ml^{-1}) was scanned. The DE-EID CT scan used 40 kVp, 50 mA, and 25 ms for one x-ray tube and 50 kVp with Cu (0.1 mm) filtering, 80 mA, and 12.5 ms exposures for the second x-ray tube. A delay of 100 ms was kept between the exposures of the two x-ray tubes to avoid cross-scatter. A total of 720 projections for each energy were acquired over a single 360° rotation. As previously mentioned, the DE-EID projection data was corrected for beam hardening prior to reconstruction. For the PCD CT scans, we used 80 KVp (with 0.1 mm Cu filtering), 2 mA, 200 ms/exposure with 900 projections acquired over a 1.25 cm vertical translation and three full rotations (helical acquisition, pitch = 0.1). The radiation dose was 162 mGy for DE-EID and 43 mGy for PCD CT. Thus, the radiation dose comparison between the two imaging procedures shows that the PCD scanning was achieved with ~3.8 times less radiation dose compared to DE-EID CT.

2.8. *In vivo* experiments

In vivo experiments were conducted in accordance with the governing protocol approved by the Institutional Animal Care and Use Committee of Duke University Medical Center (protocol A251-14-10). A CT imaging-based biodistribution study was performed for Lip-Gd and Lip-I in C57BL/6 mice (n = 6). Three mice were intravenously administered with Lip-I (1.32 mg I kg^{-1}) and other three mice with Lip-Gd (0.4 mg Gd kg^{-1}). Whole body CT

Author Manuscript Author Manuscript Author Manuscript Author Manuscript

imaging was performed at 0, 1, 2, and 3 days post-injection using EID-CT to quantify the concentrations Lip-I or Lip-Gd in the blood, liver, spleen, kidneys, and muscle.

For the tumor imaging study, we used a carcinogen-induced and genetically engineered primary model of soft tissue sarcoma developed in $p53^{fl/fl}$ mice. Primary sarcoma lesions were generated in the hind limb by intramuscular delivery of adenovirus expressing Cre recombinase (Kirsch et al 2007), followed by injection of 300 μg 3-methylcholanthrene (Sigma). Tumors resembling human undifferentiated pleomorphic sarcoma developed approximately 8–12 weeks after injection. Imaging studies were initiated when tumors were palpable (> 100mg), continuing through various stages of disease progression. Three mice were intravenously administered Lip-Gd contrast agent (0.4 mg Gd kg^{-1} body weight) and imaged 3 h later with both DE-EID and PCD micro-CT (Day 0). Three days later (Day 3), the same animals were injected with Lip-I (1.32 mg I kg^{-1} body weight) and reimaged. The dose (mg/kg) of I and Gd contrast agents used for our *in vivo* studies are within the range of doses that we and others have used extensively in pre-clinical studies for tumor (Ghaghada et al 2011) (Badea et al 2012a) and cardiovascular imaging (Ashton et al 2014, Lee et al 2014). These dose levels have not posed safety concerns and therefore are acceptable for pre-clinical studies. Material decomposition maps were computed and analyzed for *in vivo* separation and quantification of I and Gd concentrations.

The I and Gd maps resulting from the decomposition at Day 3 were used to compute two metrics for functional characterization of tumor vasculature—fractional blood volume (FBV) using Lip-I and tumor accumulated mass of nanoparticles using Lip-Gd as previously described (Clark et al 2013). FBV, which is analogous to micro-vessel density (MVD) and an indicator of tumor perfusion was computed on a whole tumor basis as follows:

$$C'_n = \begin{cases} 0, & C_n \leqslant C_b \\ C_n, & C_n > C_b \end{cases}$$

$$\mathrm{FBV} = \frac{1}{N * C_{\mathrm{Max}}} * \sum_{n=1}^{N} C'_n$$

where C_b was the threshold of detectability for Lip-I determined by measurements in the muscle of the nontumor leg, C_n and C'_n were the concentrations in voxel n before and after thresholding with C_b, N was the total number of tumor voxels, and where C_{Max} was the blood pool concentration of iodine measured in the lumen of the descending aorta.

Accumulated mass (AM), an indicator of tumor ‘leakiness’ or enhanced permeation and retention (EPR) status (Maeda 2001), measured the accumulation of Lip-Gd within tumor and was computed as follows:

$$C'_n = \begin{cases} 0, & C_n \leqslant C_b \\ C_n & C_n \leqslant C_b \end{cases}$$

Author Manuscript Author Manuscript Author Manuscript Author Manuscript

$$AM = v * \sum_{n=1}^{N} C'_n .$$

Where, C_n and C'_n were the concentrations in voxel n before and after thresholding with C_b measured as described above, and v was the volume of a single voxel.

3. Results

The simulation results for our digital phantom with its I, calcium, and Gd sections are shown by figure 2. We compare decomposition results for DE-EID, PCD2 (two materials I, Gd), and PCD4 (four materials: PE, CS, I, and Gd) decompositions. Since the DE decompositions account for only two materials (I and Gd), the calcium (corresponding to bone) mapping is incorrect (for DE-EID, calcium appears mapped as Gd and for PCD-DE, as I). This is because of an implicit assumption required for our DE decomposition of two contrast agents, namely that all positively enhancing voxels (>0 HU) are composed of I and Gd. Notably, beam-hardening correction reduced the appearance of Gd artifacts around the periphery of the phantom (only corrected results shown). Since the PCD acquisition was performed at 80 kVp with Cu filtration, the lower part of the spectrum is filtered out. Furthermore, the PCD acquisition excludes photons with a recorded energy less than 25 keV. Thus, the PCD2 and PCD4 decompositions exhibit minimal beam hardening artifacts. Since the PCD4 decomposition is a fundamental decomposition (i.e. it should be able to represent all present materials exactly), it robustly maps all material vials to their expected material maps, including the representation of calcium within the PE map. Note that the spheres in the column with the lowest concentrations of I and Gd (1 mg ml^{-1}) cannot be reliably distinguished in PCD4 decomposition. Figure 2 also shows I and Gd RMSE values in the lower-left corners of each decomposition. We observe that I and Gd decompositions are similarly accurate for all methods, with a small advantage for the DE-EID decomposition.

Figure 3 presents CNR comparisons for the same simulation results. According to the Rose criterion (CNR > 5), DE-EID and PCD based acquisitions were able to detect both I and Gd at 10 and 5 mg ml^{-1} concentrations. However, 2.5 mg ml^{-1} of I was only detectable with the DE-EID acquisition.

Figure 4 presents the projection-based experimental validation of the threshold settings of the PCD. We measured a 51% increase in contrast for Gd at 50 keV relative to 34 keV; similarly, the contrast increase for I was 20% at ~34 keV relative to 25 keV. Our simple experiment confirms that the setting of the thresholds is correct.

In figures 5 and 6 we present the results of the physical phantom experiments and compare material decomposition results for DE-EID and PCD scans. In general, all vials containing I and Gd are visible and correctly identified in terms of material for all decompositions. As indicated earlier, the condition numbers for the normalized sensitivity matrices were 4.9 for DE-EID and 37.9 for PCD4, suggesting a more difficult problem and potentially higher noise amplification for PCD spectral decomposition.

Author Manuscript Author Manuscript Author Manuscript Author Manuscript

The 3D printed PLA phantom appears in the PCD2 decomposition as a small constant bias in the I map. This is due to the fact that PLA is denser than water (HU value > 0), resulting in apparent positive concentrations of contrast material, similar to calcium in the simulation experiments. A similar small constant bias appears in the DE-EID but on the Gd map. Finally, PCD-based decomposition to 4 material maps (I, Gd, PE, and CS) appears to provide a good visual representation of the phantom. We focus next on a comparison of DE-EID and PCD4 results. The RMSE of I was 0.26 mg ml^{-1} in the DE-EID and 0.46 mg ml^{-1} in the PCD decompositions. For Gd, the RMSE was 0.25 mg ml^{-1} for DE-EID and 0.37 mg ml^{-1} for the PCD decompositions. Thus, similar to the simulation results, DE-EID CT provided slightly more accurate I and Gd decompositions. This is also apparent in the plots of measured versus true concentrations presented in figure 6. Analysis of CNR in material maps indicates better performance for DE-EID decomposition compared to PCD decomposition. For example, CNR computed for the 2 mg ml^{-1} I vial was 10.65 for DE-EID CT and 8.4 for PCD CT; similarly, the 2.5 mg ml^{-1} Gd vial had a CNR of 8.01 for DE-EID CT and 7.72 for PCD CT. This finding is not surprising since the PCD decomposition had a significantly higher condition number compared to the DE-EID decomposition. Moreover, by setting the threshold at 25 keV we have rejected some of the photons arriving at the PCD detector, which may be also a reason for the reduced CNR. Note that the experimental CNR values appear to be slightly better than in our simulations, and according to Rose criterion, are detectable. This is likely because the simulation CNR values were measured within and averaged over spheres of small diameter (1.0—2.5 mm), while these physical phantom measurements were taken in larger vials.

The biodistribution study in six C57BL/6 mice showed uptake and systemic clearance routes for Lip-I and Lip-Gd, consistent with our previously published results (figure 7) (Mukundan et al 2006). The liposomal contrast agents demonstrated the classical NP biodistribution profile: long circulating blood-pool characteristics with clearance primarily via the organs of the reticulo-endothelial system, namely the liver and spleen. The blood half-lives assuming a first order clearance rate constant, were approximately 46.5 h for Lip-I and 48 h for Lip-Gd.

Figure 8 shows examples from our *in vivo* tumor imaging experiments at Day 3 and compares reconstructed DE-EID and PCD CT axial slices and their corresponding material decompositions. Note that our reconstruction achieves low levels of noise while maintaining contrast characteristics for different energies. Material decomposition results for the sarcoma tumor imaging experiments are also shown for DE-EID CT (figure 9) and PCD CT (figure 10) at Day 0, containing only Lip-Gd, and Day 3, containing both Lip-Gd and Lip-I contrast agents. To better visualize the continuity of structures, we present maximum intensity projections (MIPs) over a volume in both axial and coronal orientations. A comparison of rendered volumes corresponding to Day 3 for DE-EID CT and PCD-CT is shown in the supplementary movies available at stacks.iop.org/PMB/64/065007/mmedia.

At Day 3 (3 d after administration of Lip-Gd), Lip-Gd is cleared from the vascular compartment and accumulates in the liver and spleen due to its systemic clearance via these organs. Additionally, the NP contrast agent accumulates in the sarcoma tumor due to the enhanced permeability and retention (EPR) effect (Maeda 2001). However, Lip-I is expected to be in the vascular compartment since imaging was performed shortly after administration

Author Manuscript Author Manuscript Author Manuscript Author Manuscript

of the agent, enabling the visualization of blood vessels. At Day 0, just after the Lip-Gd injection, the Lip-Gd concentration in the blood, determined from PCD CT, was 4.28 mg ml $^{-1}$. We note vascular enhancement in the tumor. At Day 3, both vasculature (via the I map, shown in red) and tumor EPR via Lip-Gd accumulation (green) are clearly visible.

The DE-EID results in figures 8 and 9 show post-image processing errors around the structure edges (such as bones) caused by small imperfections in registration between the two energy scans. Furthermore, the mouse soft tissue appears to contain some Gd background as a result of the only two materials decomposition. PCD results shown in figures 8 and 10 appear to be superior in quality to DE-EID results, with a cleaner soft tissue background and without artifacts caused by registration imperfections, since all four energy maps are acquired at the same time and with the same geometry. PCD-CT was able to clearly separate Gd signal (EPR-based tumor accumulation) from I signal (vascular compartment). Furthermore, the ability to decompose PE and CS maps enables the separation of bone from contrast material. In figure 11, we compare MIPs based on material decompositions from DE-EID and PCD-CT in two additional sarcoma-bearing mice imaged at Day 0 and Day 3. Functional metrics of tumor vasculature i.e. FBV measured using Lip-I and AM using Lip-Gd, were determined at Day 3 for both DE-EID and PCD-CT. Note that the two modalities provide similar values for these measures.

4. Discussion and conclusions

Micro-CT imaging plays a major role in the preclinical study of clinically-relevant pathologies. Advances in preclinical CT contrast agents have expanded the role of micro-CT from anatomic imaging to interrogating the role of vasculature in various disease models. The advent of spectral capabilities in micro-CT have further empowered the modality to extract *in vivo* functional and quantitative information about disease progression and treatment response using multiple contrast agents for simultaneous physiological and molecular imaging. Additionally, the quantitative nature of the modality facilitates conduct of preclinical studies with a strong potential for clinical translation.

In this work, we compared two spectral micro-CT imaging methods for *in vivo* preclinical cancer imaging: DE-EID and PCD-based micro-CT using NPs based on I and Gd. Overall, PCD CT with a fundamental decomposition into PE, CS, I, and Gd provided lower background signal, was not significantly affected by beam hardening, and eliminated any potential for misregistration artifacts between energies, providing cleaner *in vivo* decomposition results in spite of a higher condition number. However, we acknowledge that the DE-EID results can be improved by improving registration between imaging chains and reducing calcium blooming via model-based reconstruction. Such corrections are under investigation.

A limitation of the present study is that the radiation dose was not the same for the DE-EID and PCD scans for an objective comparison. However, according to the Rose criterion (CNR > 5) applied to the experimental results (see figure 5), the detectability limits were approximately 2.5 mg ml^{-1} for both DE-EID CT and PCD CT, even if the radiation dose was approximately 3.8 times lower with PCD CT.

Author Manuscript Author Manuscript Author Manuscript Author Manuscript

Although we have demonstrated visualization of Gd with a NP formulation containing ~5.5 times lower Gd concentration (20 mg ml^{-1}) compared to I (110 mg ml^{-1}), higher Gd concentration would be beneficial for spectral CT imaging. Notably, iterative reconstruction was extremely beneficial in providing low noise reconstruction results for improved low concentration detectability of Gd, and was applied equivalently to both the EID and PCD data.

Our spectral imaging methods could be useful for non-invasive, simultaneous visualization of multiple *in vivo* targets as well as to study the *in vivo* fate and distribution of multiple NPs. Furthermore, the ability to spectrally separate contrast agent elements (I, Gd) from calcium would be useful for molecular imaging and quantifying delivery of NPs in bone pathologies. The accuracy and sensitivity limits of this method are being explored together with more sophisticated spectral reconstruction methods. In the long term, preclinical spectral CT systems such as ours could serve for developing NPs that show promise in the field of cancer theranostics (therapy and diagnostics). Liposome formulations similar to Lip-I and Lip-Gd are also used to deliver chemotherapy (e.g. Doxil). As shown by figure 11, spectral CT can be used to simultaneously and quantitatively evaluate functional metrics of tumor vasculature i.e. tumor's fractional blood volume (FBV) and tumor 'leakiness' determined by measuring accumulated mass (AM) of nanoparticle contrast agent. The measurement of accumulated mass using Lip-Gd also serves as a surrogate for quantifying intratumoral distribution patterns of liposomal chemotherapeutics. By being fast, cost-effective, and widespread, spectral micro-CT offers the ideal imaging method for theranostics probes based on high-*Z*, K-edge materials.

Supplementary Material

Refer to Web version on PubMed Central for supplementary material.

Acknowledgments

All work was performed at the Duke Center for *In vivo* Microscopy and was supported by the NIH National Cancer Institute (R01 CA196667, U24 CA220245). Support was also provided by an NIH training Grant, T32-EB001040. This work was made possible by the loan of a SANTIS 0804 ME photon counting x-ray detector prototype from DECTRIS AG of Baden-Dättwil, Switzerland (https://www.dectris.com/). Special thanks to Drs Spyridon Gkoumas and Thomas Thuering for the installation of the photon counting x-ray detector prototype and for technical support. We would also like to acknowledge Dr David Kirsch for providing mice and Dr Yi Qi for help with the animal experiments.

References

Alvarez RE and Macovski A 1976 Energy-selective reconstructions in x-ray computerized tomography Phys. Med. Biol 21 733–44 [PubMed: 967922]

Anderson N, Butler A, Scott N, Cook N, Butzer J, Schleich N, Firsching M, Grasset R, De Ruiter N and Campbell M 2010 Spectroscopic (multi-energy) CT distinguishes iodine and barium contrast material in MICE Eur. Radiol 20 2126–34 [PubMed: 20309554]

Annapragada AV, Hoffman E, Divekar A, Karathanasis E and Ghaghada KB 2012 High-resolution CT vascular imaging using blood pool contrast agents Method. Debakey Cardiovasc. J 8 18–22

Ashton JR, Befera N, Clark D, Qi Y, Mao L, Rockman HA, Johnson GA and Badea CT 2014 Anatomical and functional imaging of myocardial infarction in mice using micro-CT and eXIA 160 contrast agent Contrastes Media Mol. Imaging 9 161–8

Author Manuscript Author Manuscript Author Manuscript Author Manuscript

Ashton JR, Castle KD, Qi Y, Kirsch DG, West JL and Badea CT 2018 Dual-energy CT imaging of tumor liposome delivery after gold nanoparticle-augmented radiation therapy Theranostics 8 1782–97 [PubMed: 29556356]

Ashton JR, Hoye J, Deland K, Whitley M, Qi Y, Moding E, Kirsch DG, West J and Badea CT 2016 A dual energy CT study on vascular effects of gold nanoparticles in radiation therapy SPIE Medi. Imaging 9788 97880W

Ashton JR, West JL and Badea CT 2015 In vivo small animal micro-CT using nanoparticle contrast agents Frontiers Pharmacol. 6 256

Badea CT, Athreya KK, Espinosa G, Clark D, Ghafoori AP, Li Y, Kirsch DG, Johnson GA, Annapragada A and Ghaghada KB 2012a Computed tomography imaging of primary lung cancer in mice using a liposomal-iodinated contrast agent PLoS One 7 e34496 [PubMed: 22485175]

Badea CT, Guo X, Clark D, Johnston SM, Marshall C and Piantadosi C 2012b Lung imaging in rodents using dual energy micro-CT Proc SPIE 8317 83171I

Badea CT, Holbrook M, Clark DP and Ghaghada K 2018 Spectral imaging of iodine and gadolinium nanoparticles using dual-energy CT SPIE Med. Imaging 10573 105731I

Badea CT, Johnston SM, Qi Y, Ghaghada K and Johnson GA 2011 Dual energy micro-CT imaging for differentiation of iodine and gold-based nanoparticles Med. Imaging 7961 79611X

Badea C, Johnston S, Johnson B, Lin M, Hedlund L and Johnson GA 2008 A dual micro-CT system for small animal imaging Med. Imaging 6913 691342

Ballabriga R, Campbell M, Heijne E, Llopart X and Tlustos L 2006 The Medipix3 prototype, a pixel readout chip working in single photon counting mode with improved spectrometric performance IEEE Nuclear Science Symp. Conf. Record vol 6 pp 3557–61

Clark DP and Badea CT 2017 Hybrid spectral CT reconstruction PLoS One 12 e0180324 [PubMed: 28683124]

Clark DP, Ghaghada K, Moding EJ, Kirsch DG and Badea CT 2013 *In vivo* characterization of tumor vasculature using iodine and gold nanoparticles and dual energy micro-CT Phys. Med. Biol 58 1683–704 [PubMed: 23422321]

Clark D, Touch M, Barber W and Badea C 2015 Simultaneous imaging of multiple contrast agents using full-spectrum micro-CT Med. Imaging 9412 941222

Gao H, Yu H, Osher S and Wang G 2011 Multi-energy CT based on a prior rank, intensity and sparsity model (PRISM) Inverse Probl. 27

Ghaghada KB, Badea CT, Karumbaiah L, Fettig N, Bellamkonda RV, Johnson G and Annapragada A 2011 Evaluation of tumor microenvironment in an animal model using a nanoparticle contrast agent in computed tomography imaging Acad. Radiol 18 20–30 [PubMed: 21145026]

Ghaghada KB, Sato AF, Starosolski ZA, Berg J and Vail DM 2016 Computed tomography imaging of solid tumors using a liposomal-iodine contrast agent in companion dogs with naturally occurring cancer PLoS One 11 e0152718 [PubMed: 27031614]

Ghaghada K, Hawley C, Kawaji K, Annapragada A and Mukundan S Jr 2008 T1 relaxivity of core-encapsulated gadolinium liposomal contrast agents—effect of liposome size and internal gadolinium concentration Acad. Radiol 15 1259–63 [PubMed: 18790397]

Gierada DS and Bae KT 1999 Gadolinium as a CT contrast agent: assessment in a porcine model Radiology 210 829–34 [PubMed: 10207488]

Gutjahr R, Halaweish AF, Yu Z, Leng S, Yu L, Li Z, Jorgensen SM, Ritman EL, Kappler S and McCollough CH 2016 Human imaging with photon counting-based computed tomography at clinical dose levels: contrast-to-noise ratio and cadaver studies Invest. Radiol 51 421–9 [PubMed: 26818529]

Kirsch DG et al. 2007 A spatially and temporally restricted mouse model of soft tissue sarcoma Nat. Med 13 992–7 [PubMed: 17676052]

Lee CL, Min H, Befera N, Clark D, Qi Y, Das S, Johnson GA, Badea CT and Kirsch DG 2014 Assessing cardiac injury in mice with dual energy-MicroCT, 4D-MicroCT, and MicroSPECT imaging after partial heart irradiation Int. J. Radiat. Oncol. Biol. Phys 88 686–93 [PubMed: 24521682]

Li Z, Leng S, Yu Z, Kappler S and McCollough CH 2016 Estimation of signal and noise for a whole-body photon counting research CT system Proc. SPIE 9783 023505

Author Manuscript Author Manuscript Author Manuscript Author Manuscript

Maeda H 2001 The enhanced permeability and retention (EPR) effect in tumor vasculature: the key role of tumor-selective macromolecular drug targeting Adv. Enzyme Regul 41 189–207 [PubMed: 11384745]

Muenzel D et al. 2017 Spectral photon-counting CT: initial experience with dual-contrast agent K-Edge colonography Radiology 283 722–7

Mukundan S Jr, Ghaghada KB, Badea CT, Kao CY, Hedlund LW, Provenzale JM, Johnson GA, Chen E, Bellamkonda RV and Annapragada A 2006 A liposomal nanoscale contrast agent for preclinical CT in mice AJR Am. J. Roentgenol 186 300–7 [PubMed: 16423931]

Radicci V, Commichau S, Donath T, Rissi M, Sakhelashvili T, Schneebeli M, Traut S, Trueb P, Tudosie G and Broennimann C First PILATUS3 200K-W CdTe detector: calibration and performance. Int. Workshop on Radiation Imaging Detectors iWoRID 2014 (Trieste, Italy 22–26 June 2014)

Rose A 1948 The sensitivity performance of the human eye on an absolute scale J. Opt. Soc. Am 38 196–208 [PubMed: 18901781]

Schlomka JP et al. 2008 Experimental feasibility of multi-energy photon-counting K-edge imaging in pre-clinical computed tomography Phys. Med. Biol 53 4031–47 [PubMed: 18612175]

Siewerdsen JH, Waese AM, Moseley DJ, Richard S and Jaffray DA 2004 Spektr: a computational tool for x-ray spectral analysis and imaging system optimization Med. Phys 31 3057–67 [PubMed: 15587659]

Starosolski Z, Villamizar CA, Rendon D, Paldino MJ, Milewicz DM, Ghaghada KB and Annapragada AV 2015 Ultra high-resolution *in vivo* computed tomography imaging of mouse cerebrovasculature using a long circulating blood pool contrast agent Sci Rep. 5 10178 [PubMed: 25985192]

Symons RA et al. 2017 Feasibility of dose-reduced Chest CT with photon-counting detectors: initial results in humans Radiology 285 980–9 [PubMed: 28753389]

Taguchi K and Iwanczyk JS 2013 Vision 20/20: single photon counting x-ray detectors in medical imaging Med. Phys 40 100901 [PubMed: 24089889]

Zou W, Hunter N and Swain MV 2011 Application of polychromatic microCT for mineral density determination J. Dent. Res 90 18–30 [PubMed: 20858779]

Author Manuscript Author Manuscript Author Manuscript Author Manuscript

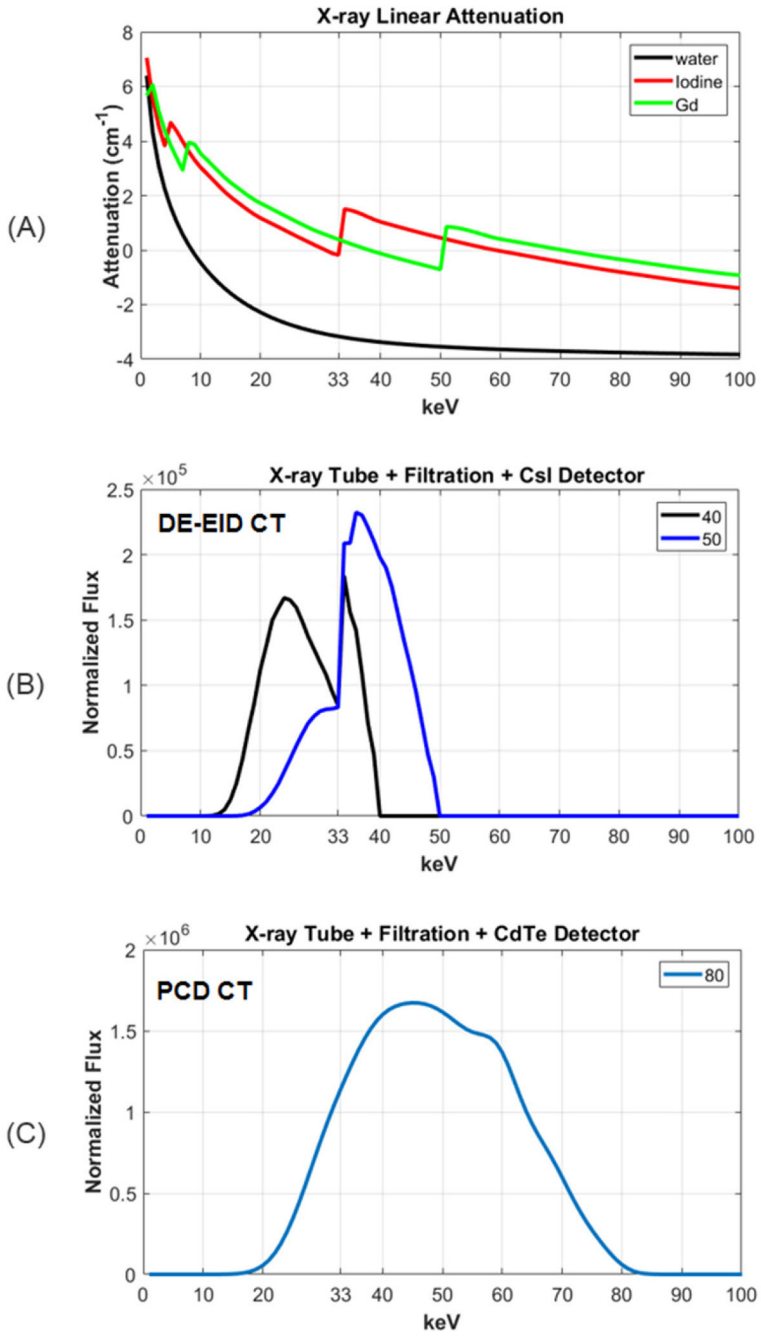

Figure 1.

(A) The attenuation coefficients for water and I and Gd solutions. Note the K-edges of I (33.2 keV) and Gd (50.2 keV). (B) The x-ray spectral response used for DE-EID simulations corresponding to 40 kVp (w/o Cu filtration) and 50 kVp (with Cu filtration). (C) The x-ray spectral response for the PCD CT with the x-ray tube scanning with 80 kVp and Cu filtration.

Author Manuscript Author Manuscript Author Manuscript Author Manuscript

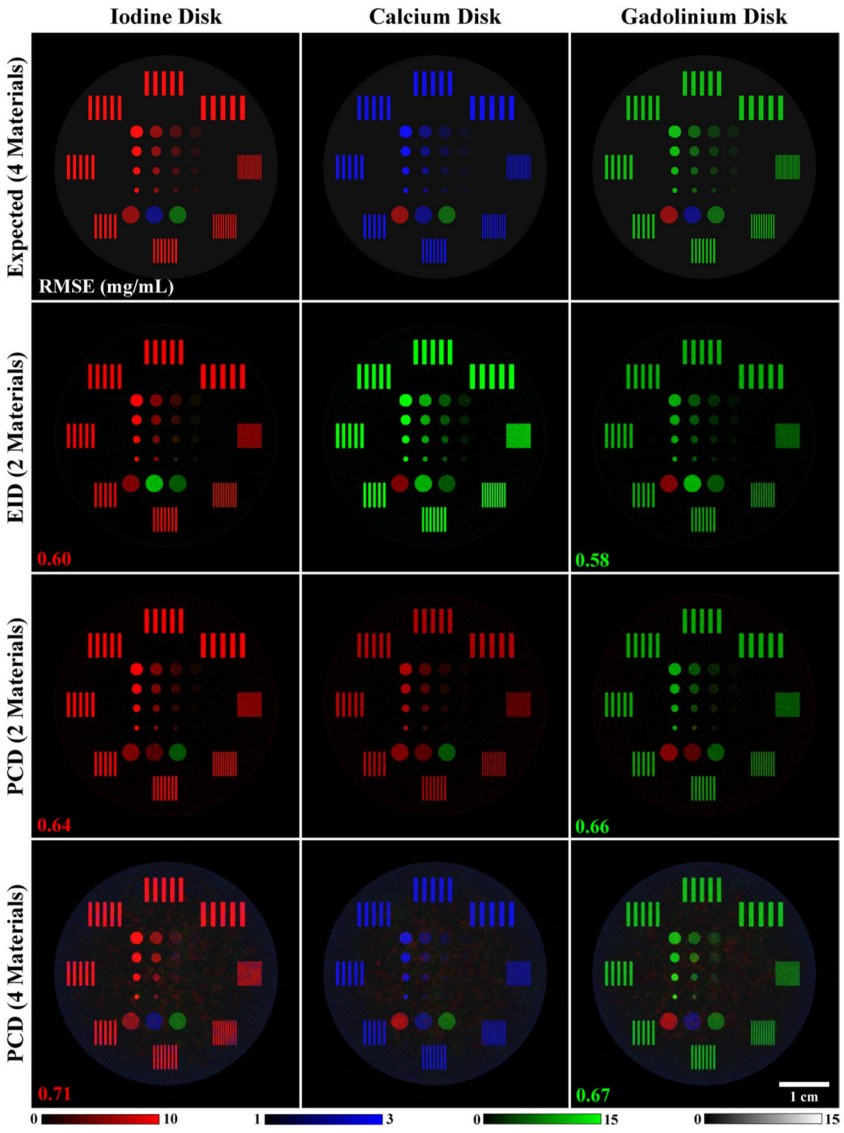

Figure 2.

Tomographic axial slices through the digital phantom (top row) with the expected material maps through the disks containing I, calcium, and Gd. The following three rows show results for material decompositions corresponding to the DE-EID, PCD2, and PCD4 cases. The I is shown in red, calcium (PE) in blue, Gd in green, and CS in gray. RMSE values computed relative to the expected values (over 50, 2D slices) are shown in the lower corner of the I and Gd images. Concentration (water fraction) windowing for each material map is shown at the bottom of the figure.

Author Manuscript Author Manuscript Author Manuscript Author Manuscript

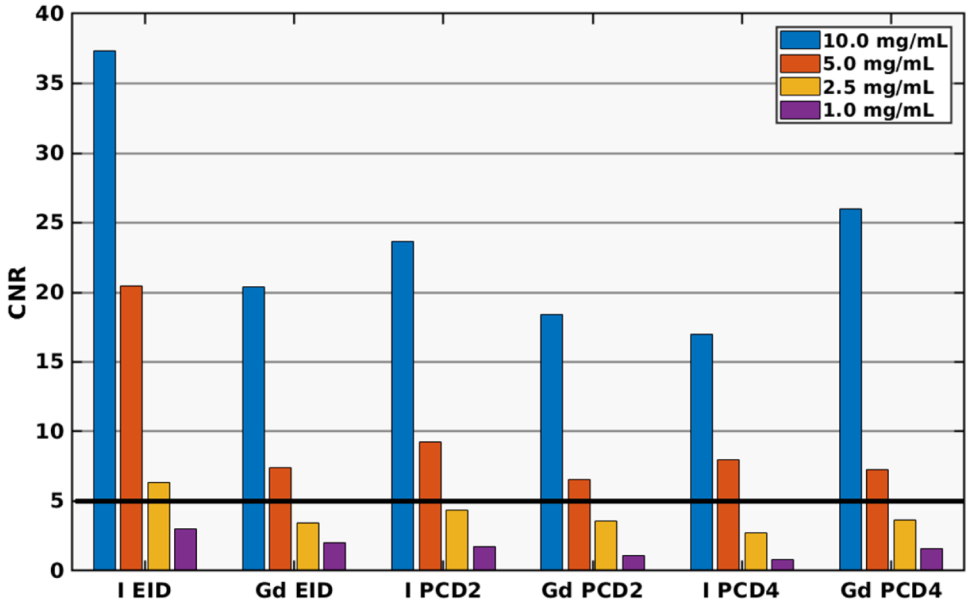

Figure 3.

Comparison of CNRs measured in the simulation studies, with concentrations per column and with CNR values averaged over all four spheres. CNRs are shown for I and Gd in the DE-EID, PCD2 (two material decomposition), and PCD4 (four material decomposition) cases. The solid horizontal line indicates CNR = 5, which was used for determining minimal detectable concentrations (Rose 1948).

Author Manuscript Author Manuscript Author Manuscript Author Manuscript

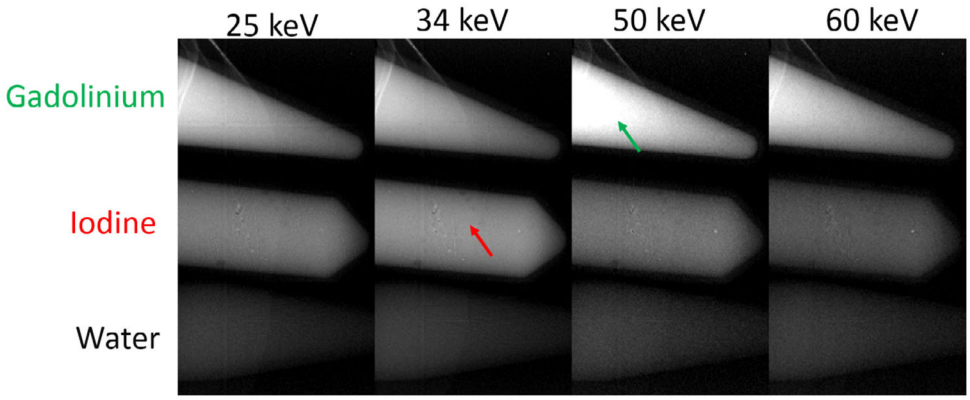

Figure 4.

Experimental validation of the PCD thresholds in a phantom containing vials with I and Gd solutions in water. Projections are compared following water normalization. There is a clear increase in contrast for Gd at ~50 keV. The contrast enhancement of I is less prominent at ~34 keV. These projections were not subtracted between the consecutive energy thresholds.

Author Manuscript Author Manuscript Author Manuscript Author Manuscript

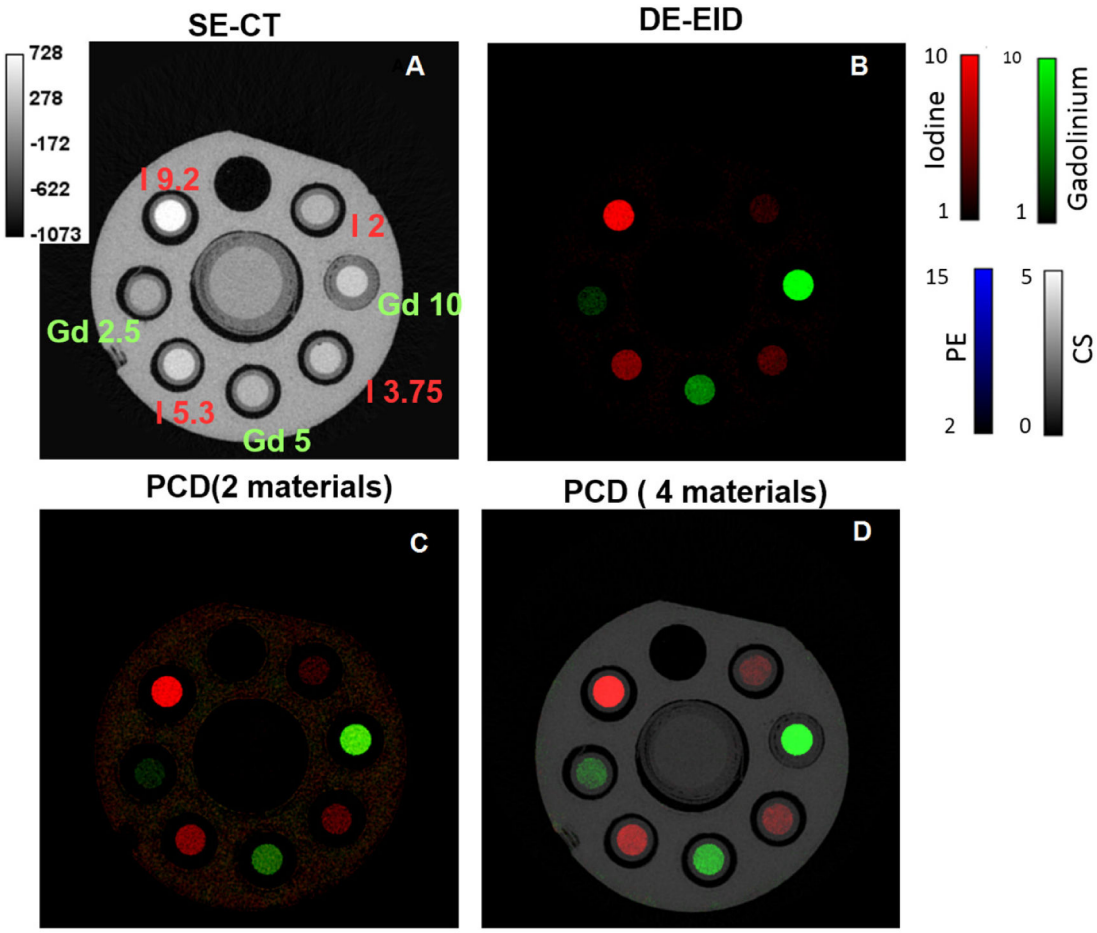

Figure 5.

The phantom (A) and the material decomposition maps for DE-EID(B) PCD (two materials) (C) and PCD four materials (D). I vials appear in red and Gd vials appear in green.

Author Manuscript Author Manuscript Author Manuscript Author Manuscript

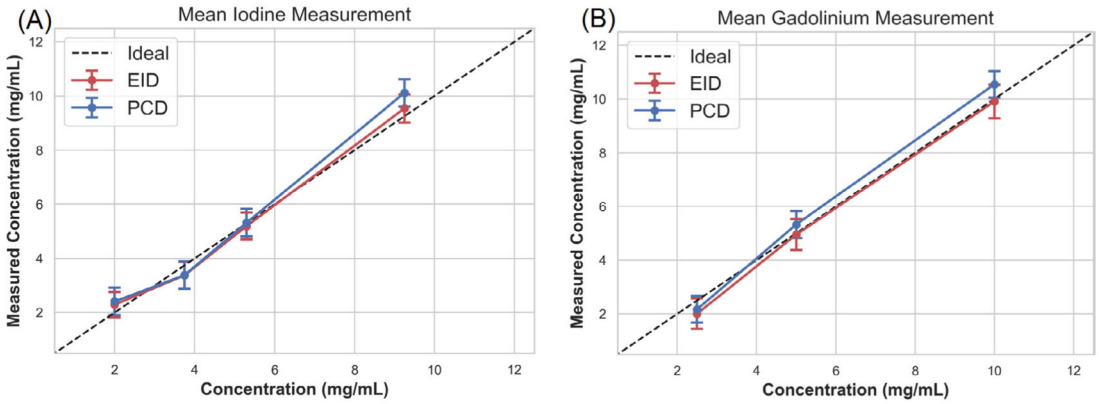

Figure 6.

The plots of measured versus true concentrations for all vials in the phantom containing I (A) and Gd (B) for DE-EID and PCD (four materials) CT. The bars represent standard deviations of the measured concentrations.

Author Manuscript Author Manuscript Author Manuscript Author Manuscript

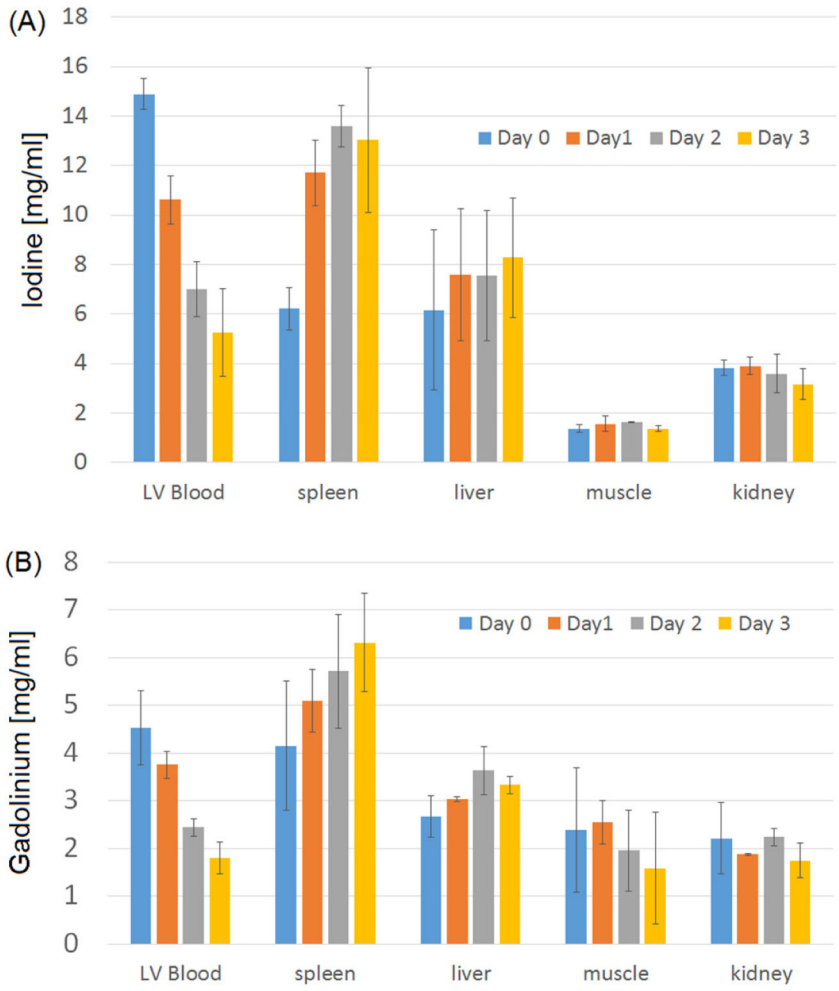

Figure 7.

The biodistribution of Lip-I (A) and Lip-Gd (B) illustrated in the plots of the mean values for the uptake of Lip-I ($n = 3$ mice) and Lip-Gd ($n = 3$ mice) in blood and target organs over 4 d. The error bars represent the standard deviation of concentrations.

Author Manuscript Author Manuscript Author Manuscript Author Manuscript

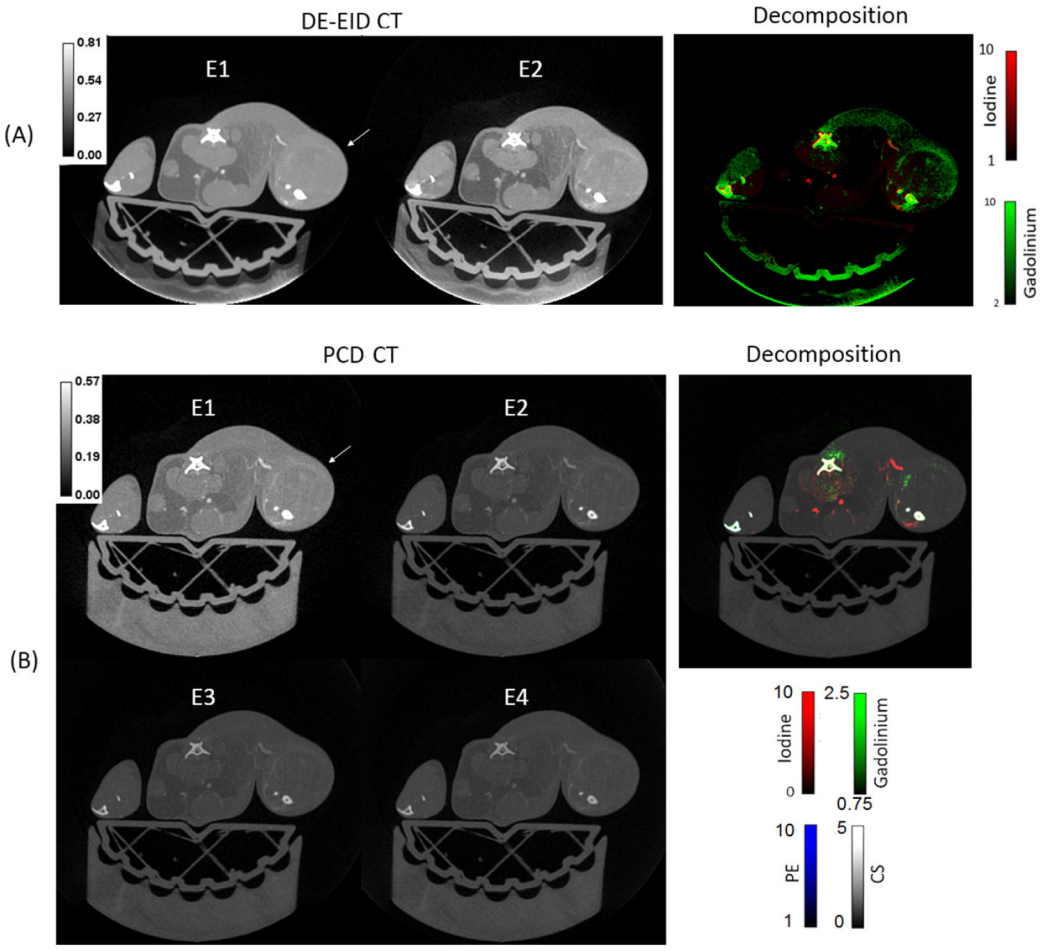

Figure 8.

Examples of DE-EID CT (A) and PCD CT (B) axial reconstructed slices at different energies and their material decomposition maps at Day 3. The sarcoma tumor is positioned on the leg and is indicated by white arrows. The values in the color bars are in (1/cm) for the reconstructed images and in (mg ml^{-1}) (I, Gd) and (water fraction) (PE, CS) for the material decompositions.

Author Manuscript Author Manuscript Author Manuscript Author Manuscript

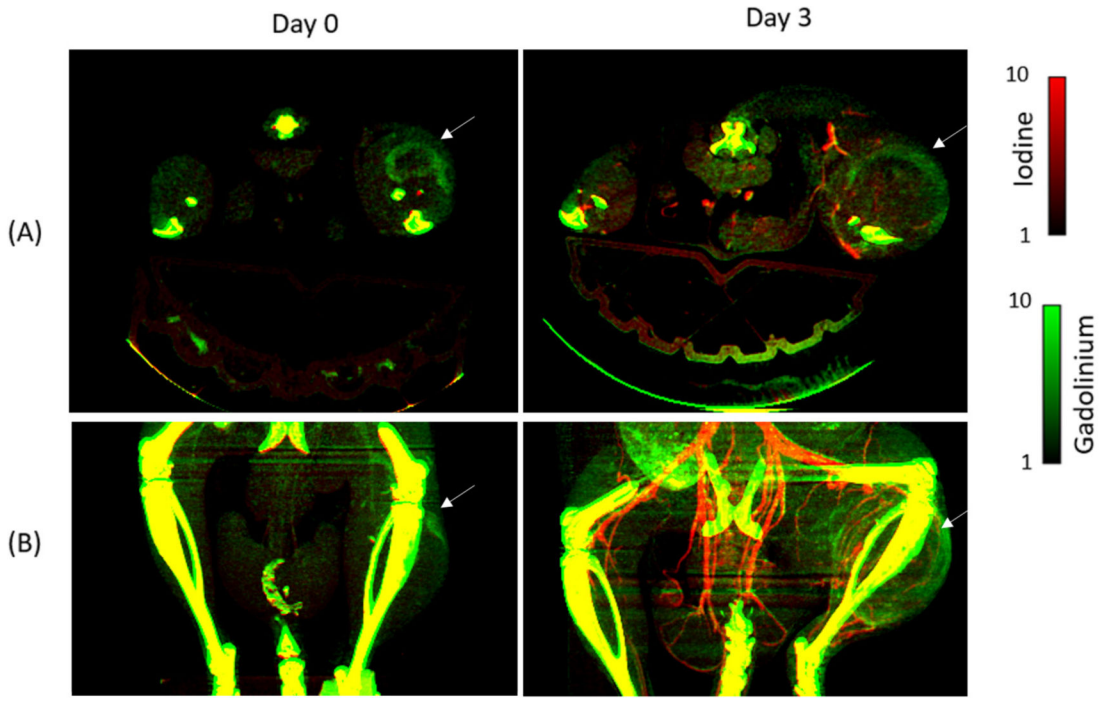

Figure 9.

MIPs based on DE-EID CT decompositions of a mouse with a sarcoma tumor (white arrows) in axial (A) and coronal (B) orientations at Day 0 and Day 3.

Author Manuscript Author Manuscript Author Manuscript Author Manuscript

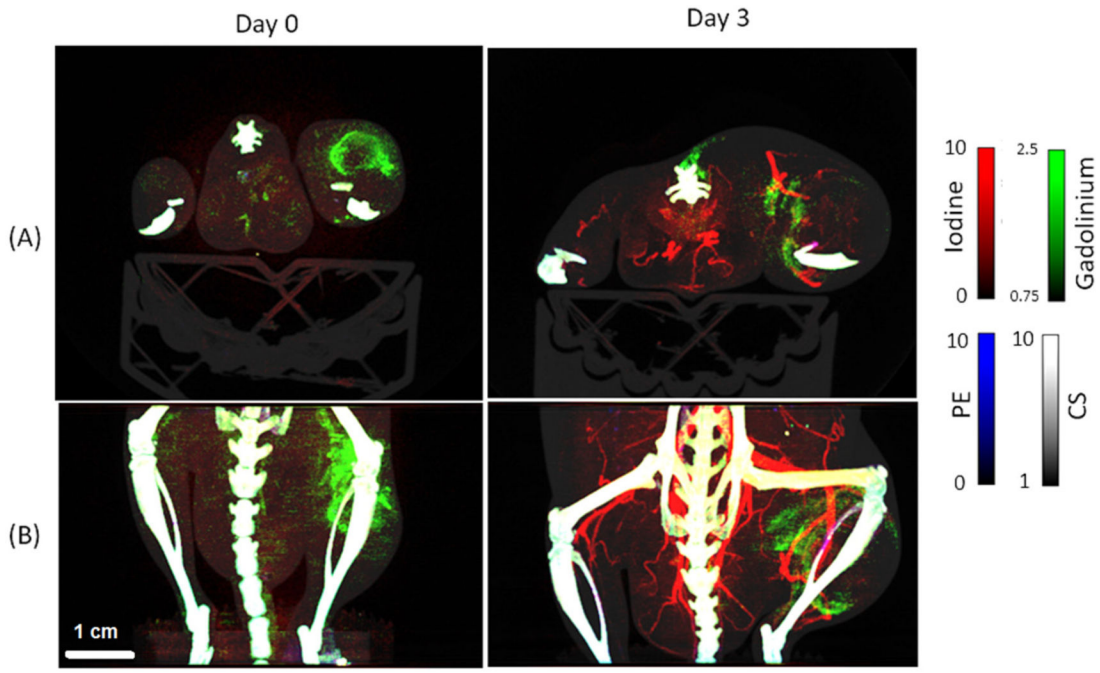

Figure 10.
MIPs based on PCD CT decompositions of a mouse with a sarcoma tumor in axial (A) and coronal (B) orientations at Day 0 and Day 3.

Author Manuscript Author Manuscript Author Manuscript Author Manuscript

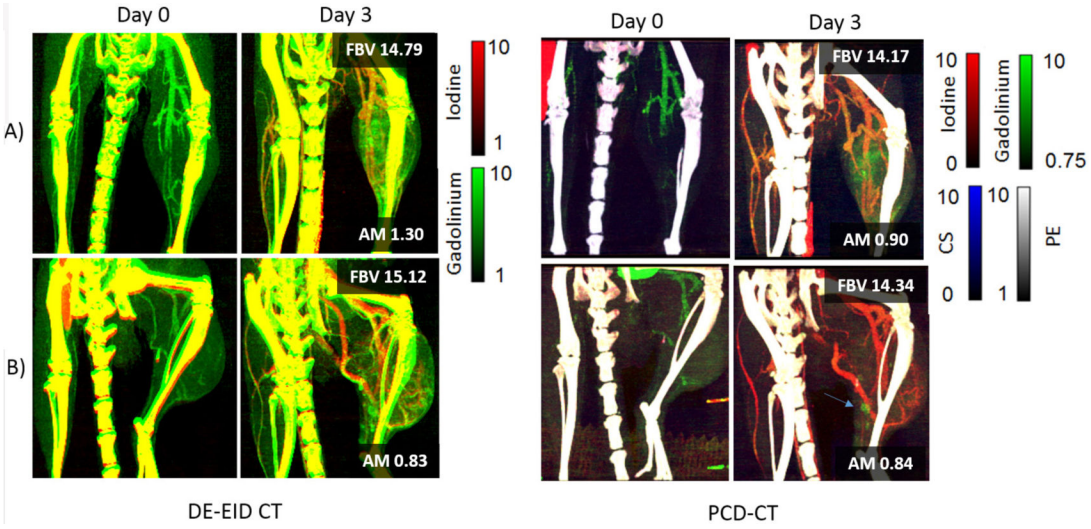

Figure 11.

MIP decomposition comparison in two different mice (A) and (B) for Day 0 and Day 3 with DE-EID (left) and PCD-CT (right). For each mouse, fractional blood volume (FBV) and accumulated mass (AM) were computed using Lip-I and Lip-Gd, respectively at Day 3.